

# Implications of the fermion vacuum term in the extended SU(3) quark meson model on compact star properties

Andreas Zacchi<sup>\*</sup> and Jürgen Schaffner-Bielich<sup>†</sup>

*Institut für Theoretische Physik, Goethe Universität Frankfurt,  
Max von Laue Strasse 1, D-60438 Frankfurt, Germany*

 (Received 4 October 2019; published 30 December 2019)

We study the impact of the fermion vacuum term in the SU(3) quark meson model on the equation of state and determine the vacuum parameters for various sigma meson masses. We examine its influence on the equation of state and on the resulting mass radius relations for compact stars. The tidal deformability  $\Lambda$  of the stars is studied and compared to the results of the mean field approximation. Parameter sets which fulfill the tidal deformability bounds of GW170817 together with the observed two solar mass limit turn out to be restricted to a quite small parameter range in the mean field approximation. The extended version of the model does not yield solutions fulfilling both constraints. Furthermore, no first order chiral phase transition is found in the extended version of the model, not allowing for the twin star solutions found in the mean field approximation.

DOI: [10.1103/PhysRevD.100.123024](https://doi.org/10.1103/PhysRevD.100.123024)

## I. INTRODUCTION

The theory of the strong interaction, quantum chromodynamics (QCD), describes the interaction between quarks and gluons. The QCD Lagrangian possesses an exact color and flavor symmetry for  $N_f$  massless quark flavors [1–6], and chiral symmetry controls the hadronic interactions in the low energy regime [7,8]. At high temperatures or densities chiral symmetry is expected to be restored [2,9,10]. The possible appearance of quark matter at high densities has interesting consequences for the properties of compact stars [11–18].

Since QCD cannot be solved on the lattice at nonzero density, effective models are needed to study the features and interactions of high density matter [5,19–23]. The chiral SU(3) quark meson model is a well established and studied framework [5,23–34]. Its advantage in comparison to other chiral models such as the Nambu-Jona-Lasinio model [35–38] lies in its renormalizability [31,32,39] by taking into account vacuum fluctuations.

In this article we study the impact of the fermion vacuum term on the equation of state (EoS) in the SU(3) quark meson model in an extended mean field approximation (eMFA); see also [20,28,40–43]. For that purpose we determine the vacuum parameters for different sigma meson masses  $m_\sigma$ . The dependence of the vacuum parameters on the renormalization scale parameter  $\Lambda_r$  cancels with the dependence of the additional fermion vacuum term  $\Omega_{qq}^{\text{vac}}(\Lambda_r)$  in the grand potential, so that the whole grand potential is independent of the renormalization scale parameter  $\Lambda_r$  [28,31,42,43].

The resulting EoSs are investigated and subsequently used to solve the Tolman–Oppenheimer–Volkoff (TOV) equations [44] for various parameters of the model, that is, the sigma meson mass  $m_\sigma$ , the repulsive vector coupling constant  $g_\omega$ , and the vacuum pressure constant  $B^{1/4}$ . Constraints on the EoS for compact stars are imposed by the observation of the  $2 M_\odot$  neutron stars [45–48] and by the gravitational wave measurement GW170817 [49,50] of a binary neutron star merger. In this context, the tidal deformability parameter  $\Lambda$  depends on the compactness  $C$  of the compact star and on the Love number  $k_2$  [51–53] via

$$\Lambda = \frac{2k_2}{3C^5}. \quad (1)$$

The GW170817 measurement on the tidal deformability deduces  $\Lambda = 300_{-230}^{+420}$  for a  $1.4 M_\odot$  star [50]. Inferred from that measurement, the radius of a  $1.4 M_\odot$  star cannot be larger than  $R \geq 13.5$  km [54–61].

The mass radius relations of the eMFA are compared to those of the standard mean field approximation (MFA). We find that the mass radius relations for a given parameter set in the eMFA are in general less compact compared to the MFA case. Less compact star configurations imply rather large values of the tidal deformability parameter  $\Lambda$ . Fulfilling all considered constraints on mass  $M \geq 2 M_\odot$ , radius  $R \leq 13.5$  km at  $1.4 M_\odot$ , and the tidal deformability parameter  $\Lambda \leq 720$  for a  $1.4 M_\odot$  star is possible in a narrow parameter space for the MFA. The parameters in the eMFA do not allow for solutions which satisfy the above-mentioned constraints.

Further analysis of the parameter range of the SU(3) chiral quark meson model in the eMFA exhibits that the

<sup>\*</sup>zacchi@astro.uni-frankfurt.de

<sup>†</sup>schaffner@astro.uni-frankfurt.de

inclusion of the fermion vacuum term yields crossover transitions from a chirally broken phase to a restored phase exclusively. This feature consequently smooths the EoSs compared to the MFA case not allowing for twin star solutions, that is, two stable branches in the mass radius relation, as found for a certain parameter range in the MFA (see, e.g., [18]).

## II. THE SU(3) QUARK MESON MODEL

A chirally invariant model with three flavors  $N_f = 3$  and with quarks as the active degrees of freedom is the SU(3) chiral quark meson model. Based on the theory of the strong interaction, an effective model must doubtlessly implement features of QCD, such as flavor symmetry and spontaneous and explicit breaking of chiral symmetry. The  $N_f = 3$  Lagrangian [6,16,32,62] respecting these symmetries and including vector mesonic interactions reads

$$\begin{aligned} \mathcal{L} = & \sum_{\alpha} \bar{\Psi}_n (i\partial - g_{\alpha} m_n) \Psi_n + \bar{\Psi}_s (i\partial - g_{\alpha} m_s) \Psi_s \\ & + \text{tr}(\partial_{\mu} \Phi)(\partial^{\mu} \Phi)^{\dagger} - \lambda_1 [\text{tr}(\Phi^{\dagger} \Phi)]^2 - \lambda_2 \text{tr}(\Phi^{\dagger} \Phi)^2 \\ & + \text{tr}[\hat{H}(\Phi + \Phi^{\dagger})] + c(\det(\Phi^{\dagger}) + \det(\Phi)) \\ & - m_0^2(\text{tr}(\Phi^{\dagger} \Phi)) - m_v^2 \text{tr}(V^{\dagger} V) \end{aligned} \quad (2)$$

with a Yukawa-like coupling  $g_{\alpha}$ ,  $\alpha$  being the fields  $\sigma_n$ ,  $\sigma_s$ ,  $\omega$ ,  $\rho$ , and  $\phi$  involved, and the effective mass  $m_{n,s}$  to the spinors  $\Psi_{n,s}$ . The indices  $n = \text{nonstrange}$  and  $s = \text{strange}$  indicate the flavor content. All physical fields are arranged in the matrix  $\Phi$  [5,6]

$$\Phi = \frac{1}{\sqrt{2}} \begin{pmatrix} \frac{(\sigma_n + a_0^0) + i(\eta_n + \pi_0)}{\sqrt{2}} & a_0^+ + i\pi^+ & K_s^+ + iK^+ \\ a_0^- + i\pi^- & \frac{(\sigma_n - a_0^0) + i(\eta_n - \pi^0)}{\sqrt{2}} & K_s^0 + iK^0 \\ K_s^- + iK^- & \bar{K}_s^0 + i\bar{K}^0 & \sigma_s + i\eta_s \end{pmatrix}, \quad (3)$$

where we consider the condensed  $\sigma_{n,s}$  fields and the pions to determine the vacuum parameters  $\lambda_1$ ,  $\lambda_2$ ,  $m_0^2$ ,  $c$ ,  $h_n$ , and  $h_s$  of the model, which are fixed at tree level [27,32,62,63], but change upon renormalization [39,42,43] (see Sec. II A). In thermal equilibrium the grand potential  $\Omega$  is calculated via the partition function  $\mathcal{Z}$ , which is defined as a path integral over the fermion fields,

$$\Omega = -\frac{\ln \mathcal{Z}}{\beta} \quad \text{with } \mathcal{Z} = \int \mathcal{D}\Psi \mathcal{D}\bar{\Psi} e^{\int_0^{\beta} dt \int d^3\vec{x} \mathcal{L}}. \quad (4)$$

Evaluated, the grand canonical potential reads

$$\begin{aligned} \Omega_{\bar{q}q} &= V + \Omega_{\bar{q}q}^{\text{vac}} + \Omega_{\bar{q}q}^{\text{th}} \\ &= V - \frac{3}{\pi^2 \beta} \int_0^{\infty} k^2 dk \cdot (\mathcal{R} + \mathcal{N}), \end{aligned} \quad (5)$$

where  $V$  is the tree level potential

$$\begin{aligned} V = & \frac{\lambda_1}{4} ((\sigma_n^2 + \sigma_s^2)^2) + \frac{\lambda_2}{8} (\sigma_n^4 + 2\sigma_s^4) + \frac{m_0^2}{2} (\sigma_n^2 + \sigma_s^2) \\ & - h_n \sigma_n - h_s \sigma_s - \frac{c \sigma_n^2 \sigma_s}{2\sqrt{2}} \\ & - \frac{1}{2} (m_{\omega}^2 \omega^2 + m_{\rho}^2 \rho^2 + m_{\phi}^2 \phi^2) + B^{1/4}, \end{aligned} \quad (6)$$

where  $B^{1/4}$  is a phenomenological vacuum pressure term [64–67], which will stiffen or soften the EoS  $p(\epsilon)$ , pressure  $p$  vs energy density  $\epsilon$ . The fermion vacuum term is

$$\Omega_{\bar{q}q}^{\text{vac}} = \mathcal{R} = \frac{E_{n,s}}{T}, \quad (7)$$

and the part from the mean field approximation is

$$\begin{aligned} \Omega_{\bar{q}q}^{\text{th}} = \mathcal{N} = & \ln(1 + e^{-\beta(E_n + \tilde{\mu}_u)}) + \ln(1 + e^{-\beta(E_n - \tilde{\mu}_u)}) \\ & + \ln(1 + e^{-\beta(E_n + \tilde{\mu}_d)}) + \ln(1 + e^{-\beta(E_n - \tilde{\mu}_d)}) \\ & + \ln(1 + e^{-\beta(E_s + \tilde{\mu}_s)}) + \ln(1 + e^{-\beta(E_s - \tilde{\mu}_s)}). \end{aligned} \quad (8)$$

The dependence of  $\Omega_{\bar{q}q}^{\text{th}}$  on the chiral condensates  $\sigma_{n,s}$  is implicit in the relativistic quasiparticle dispersion relation for the constituent quarks

$$E_{n,s} = \sqrt{k^2 + \tilde{m}_{n,s}^2}. \quad (9)$$

The quantity  $\tilde{m}_{n,s} = g_{\alpha} m_{n,s}$  is the in medium mass generated by the scalar fields.  $\mu_{n,s}$  in Eq. (8) are the respective chemical potentials

$$\tilde{\mu}_{\text{up}} = \tilde{\mu}_u = g_{\omega} \omega + g_{\rho} \rho, \quad (10)$$

$$\tilde{\mu}_{\text{down}} = \tilde{\mu}_d = g_{\omega} \omega - g_{\rho} \rho, \quad (11)$$

$$\tilde{\mu}_{\text{strange}} = \tilde{\mu}_s = g_{\phi} \phi. \quad (12)$$

### A. Renormalized vacuum parameters of the SU(3) quark meson model

The implementation of the fermion vacuum term needs regularization schemes. In this work we employ the minimal subtraction scheme and follow the procedure as found in [20,28,39–43] to properly perform the regularization of the divergence. The diverging integral containing the fermion vacuum contribution in Eq. (5) is to lowest order just the one-loop effective potential at zero temperature [41] and is dimensionally regularized via the corresponding counterterm

$$\delta \mathcal{L} = \frac{N_c N_f}{16\pi^2} \tilde{m}_{n,s}^4 \left[ \frac{1}{\epsilon} - \frac{1}{2} [-3 + 2\gamma - 4 \ln(2\sqrt{\pi})] \right], \quad (13)$$

which gives

$$\Omega_{qq}^{\text{vac}} = \frac{N_c N_f}{16\pi^2} \tilde{m}_{n,s}^4 \left[ \frac{1}{\epsilon} - \frac{1}{2} \left[ -3 + 2\gamma + 4 \ln \left( \frac{\tilde{m}_{n,s}}{2\sqrt{\pi}\Lambda_r} \right) \right] \right], \quad (14)$$

where  $N_c = 3$  is the number of colors,  $\lim \epsilon \rightarrow 0$  is from dimensional reasoning,  $\gamma$  is the Euler-Mascheroni constant, and  $\Lambda_r$  is the renormalization scale parameter. The dimensionally regularized fermion vacuum contribution eventually reads

$$\Omega_{qq}^{\text{dr}} = -\frac{N_c N_f}{8\pi^2} \tilde{m}_f^4 \ln \left( \frac{\tilde{m}_{n,s}}{\Lambda_r} \right). \quad (15)$$

As in mean field approximation, the six model parameters  $\lambda_1$ ,  $\lambda_2$ ,  $m_0^2$ ,  $c$ ,  $h_n$ , and  $h_s$  are fixed by six experimentally known values [32,62,68]. As an input the pion mass  $m_\pi = 136$  MeV, the kaon mass  $m_k = 496$  MeV, the pion decay constant  $f_\pi = 92.4$  MeV, the kaon decay constant  $f_k = 113$  MeV, the masses of the eta meson  $m_\eta = 548$  MeV, the mass of the eta-prime meson  $m_{\eta'} = 958$  MeV, and the mass of the sigma meson  $m_\sigma$  need to be known.

The mass of the sigma meson  $m_\sigma$  is experimentally not well determined. Usually, the sigma meson is identified with the experimentally measured resonance  $f_0(500)$ , which is rather broad,  $400 \leq m_{f_0} \leq 600$  MeV [68,69]. In Ref. [6] it was demonstrated that within an extended quark-meson model that includes vector and axial-vector interactions, the resonance  $f_0(1370)$  could be identified as this scalar state. The mass of the sigma meson is chosen from  $400 \leq m_\sigma \leq 800$  MeV in the following.

The starting point for the determination of the vacuum parameters is the potential  $V$ , Eq. (6), including the pions and the vacuum contribution  $\Omega_{qq}$ , Eq. (7), which together form  $\mathcal{V}$ ,

$$\begin{aligned} \mathcal{V} = & \frac{\lambda_1}{4} [(\sigma_n^2 + \sigma_s^2)^2 + 2\pi_0^2(\sigma_n^2 + \sigma_s^2) + \pi_0^4] \\ & + \frac{\lambda_2}{8} [(\sigma_n^2 + \pi_0^2)^2 + 2\sigma_s^4] + \frac{m_0^2}{2} (\sigma_n^2 + \pi_0^2 + \sigma_s^2) \\ & - h_n \sigma_n - h_s \sigma_s - c \left( \frac{\sigma_n^2 \sigma_s + \pi_0^2 \sigma_s}{2\sqrt{2}} \right) + B^{1/4} \\ & + \frac{1}{2} (m_\omega^2 \omega^2 + m_\rho^2 \rho^2 + m_\phi^2 \phi^2) \\ & - \frac{N_c N_f}{8\pi^2} (\sigma_n^2 + \sigma_s^2)^2 \ln \left( \frac{g\sqrt{\sigma_n^2 + \sigma_s^2}}{\Lambda_r} \right). \end{aligned} \quad (16)$$

The procedure to determine the vacuum parameters is similar as in the SU(2) case [39]. Here, three of the six derivatives to determine the vacuum parameters read

$$\begin{aligned} h_n &= m_0^2 \sigma_n - \frac{c\sigma_s \sigma_n}{\sqrt{2}} + \lambda_1 (\sigma_n^2 + \sigma_s^2) \sigma_n + \frac{\lambda_2}{2} \sigma_n^3 + \text{Vac.}, \\ h_s &= m_0^2 \sigma_s - \frac{c\sigma_n^2}{\sqrt{2}\sqrt{2}} + \lambda_1 (\sigma_n^2 + \sigma_s^2) \sigma_s + \lambda_2 \sigma_s^3 + \text{Vac.}, \\ m_\pi^2 &= m_0^2 - \frac{c\sigma_s}{\sqrt{2}} + \lambda_1 (\sigma_n^2 + \sigma_s^2) + \frac{\lambda_2}{2} \sigma_n^2 + \text{Vac.}, \end{aligned} \quad (17)$$

with the vacuum contribution yet to be determined. Since the pion does not form a condensate, it does not occur anymore in Eqs. (17) above. Due to the mixing of the fields, the second derivative  $\partial^2 \mathcal{V} / \partial \sigma_n^2$  does not yield the mass of the sigma meson as in the two flavor case SU(2). At this point the kaon mass is needed as an input parameter and one remains with three unknown quantities [28].

It is necessary to rewrite the nonstrange-strange basis in terms of the generators, i.e., the mathematical fields, and afterwards identifying those with the physical fields. Following [32,62] the matrix  $\Phi$ , Eq. (3), can be written as  $\Phi = T_a \Phi_a = T_a (\sigma_a + i\pi_a)$  with  $T_a = \frac{\lambda_a}{2}$ ,  $\lambda_a$  being the Gell Mann matrices where  $a = 0, 1, 2, \dots, 8$  are the nine generators of the U(3) symmetry group. The generators obey the U(3) algebra with the standard symmetric  $d_{abc}$  and antisymmetric structure constants  $f_{abc}$ . Rearranging the entries of Eq. (3) gives

$$\Phi = \frac{1}{2} \begin{pmatrix} \sqrt{\frac{2}{3}}\sigma_0 + \sigma_3 + \frac{\sigma_8}{\sqrt{3}} & \sigma_1 - i\sigma_2 & \sigma_4 - i\sigma_5 \\ \sigma_1 + i\sigma_2 & \sqrt{\frac{2}{3}}\sigma_0 - \sigma_3 + \frac{\sigma_8}{\sqrt{3}} & \sigma_6 - i\sigma_7 \\ \sigma_4 + i\sigma_5 & \sigma_6 + i\sigma_7 & \sqrt{\frac{2}{3}}\sigma_0 - \frac{2\sigma_8}{\sqrt{3}} \end{pmatrix}, \quad (18)$$

and the transformation from the physical nonstrange-strange basis to the mathematical basis reads

$$\begin{pmatrix} \sigma_n \\ \sigma_s \end{pmatrix} = \frac{1}{\sqrt{3}} \begin{pmatrix} \sqrt{2} & 1 \\ 1 & -\sqrt{2} \end{pmatrix} \begin{pmatrix} \sigma_0 \\ \sigma_8 \end{pmatrix}. \quad (19)$$

Separating the entries for the scalar and the pseudoscalar sector gives the potential in terms of the mathematical fields [32,62]. The mass matrix  $m_{ij}$  is determined only by the mesonic part and by the fermionic vacuum term of the potential  $\mathcal{V}$ , Eq. (16), because the quark contribution vanishes at  $T = \mu = 0$ . Because of isospin symmetry some entries of  $m_{ij}^2$  are degenerate and furthermore  $m_{08}^2 = m_{80}^2$ , so that

$$m_{ij}^2 = \frac{\partial^2 \mathcal{V}}{\partial \Phi_i \partial \Phi_j} = \begin{pmatrix} m_{00}^2 & \dots & m_{08}^2 \\ \vdots & \ddots & \vdots \\ m_{80}^2 & \dots & m_{88}^2 \end{pmatrix}. \quad (20)$$

This matrix needs to be diagonalized for  $m_\sigma^2$  and  $m_{f_0}^2$  in the scalar sector, and for  $m_\eta$  and  $m'_\eta$  in the pseudoscalar sector introducing a mixing angle  $\theta$ . Eventually the mass of the kaon in the nonstrange-strange basis reads

$$m_k^2 = m_0^2 - \frac{c\sigma_n}{2} + \lambda_1(\sigma_n^2 + \sigma_s^2) + \frac{\lambda_2}{2}(\sigma_n^2 - \sqrt{2}\sigma_n\sigma_s + 2\sigma_s^2), \quad (21)$$

which determines the axial anomaly term to be

$$c = \frac{-2(m_k^2 - m_\pi^2) - \lambda_2(\sqrt{2}\sigma_n\sigma_s - 2\sigma_s^2)}{\sigma_n - \sqrt{2}\sigma_s}. \quad (22)$$

Using Eq. (20), the sum of  $m_\eta$  and  $m'_\eta$  reads

$$\begin{aligned} m_\eta + m'_\eta &= 2m_0^2 + 2\lambda_1(\sigma_n^2 + \sigma_s^2) + \frac{\lambda_2}{2}(\sigma_n^2 + 2\sigma_s^2) + \frac{c\sigma_s}{\sqrt{2}} \\ &= 2m_\pi^2 - \frac{\lambda_2}{2}(\sigma_n^2 - 2\sigma_s^2) + \frac{3c\sigma_s}{\sqrt{2}}, \end{aligned} \quad (23)$$

and inserting Eq. (22) into Eq. (23) to solve for  $\lambda_2$  gives

$$\lambda_2 = \frac{m_\eta^2 + m_\eta'^2 - 2m_\pi^2 + \frac{6\sigma_s(m_k^2 - m_\pi^2)}{\sqrt{2}(\sigma_n - \sqrt{2}\sigma_s)}}{\sigma_s^2 - \frac{\sigma_n^2}{2} - \frac{(3\sqrt{2}\sigma_n^2\sigma_s - 6\sigma_s^3)}{\sqrt{2}(\sigma_s - \sqrt{2}\sigma_s)}}. \quad (24)$$

The further procedure in the mean field approximation is to determine  $\lambda_1(m_0^2)$  via  $m_\sigma$  and  $m_\pi$  [16,32,62]. The quantities obtained so far enter into the two condensate equations, Eqs. (17), for the explicit symmetry breaking terms  $h_n$  and  $h_s$ . Working in the extended version of the model, the vacuum contributing a part from Eq. (16) has to be rewritten in terms of the mathematical fields. Furthermore

$$\frac{\partial^2 \Omega_{qq}^{dr}}{\partial^2 \sigma_0^2} = \kappa \left[ \mathcal{A}\mathcal{W} + \frac{\mathcal{X}(\frac{8}{3}\sigma_0 - \frac{2\sqrt{2}}{3}\sigma_8)}{\mathcal{Z}} \right], \quad (25)$$

$$\frac{\partial^2 \Omega_{qq}^{dr}}{\partial^2 \sigma_0 \sigma_8} = \kappa \left[ \mathcal{B}\mathcal{W} + \frac{\mathcal{X}(\frac{10}{3}\sigma_8 - \frac{2\sqrt{2}}{3}\sigma_0)}{\mathcal{Z}} \right], \quad (26)$$

$$\frac{\partial^2 \Omega_{qq}^{dr}}{\partial^2 \sigma_8^2} = \kappa \left[ \mathcal{C}\mathcal{W} + \frac{\mathcal{Y}(\frac{10}{3}\sigma_8 - \frac{2\sqrt{2}}{3}\sigma_0)}{\mathcal{Z}} \right], \quad (27)$$

where

$$\kappa = -\frac{N_c N_f}{72\pi^2} g^4, \quad (28)$$

$$\mathcal{A} = 96\sigma_0^2 - 48\sqrt{2}\sigma_0\sigma_8 + 48\sigma_8^2, \quad (29)$$

$$\mathcal{B} = 96\sigma_0\sigma_8 - 30\sqrt{2}\sigma_8^2 - 24\sqrt{2}\sigma_0^2, \quad (30)$$

$$\mathcal{C} = 48\sigma_0^2 - 60\sqrt{2}\sigma_8\sigma_0 + 150\sigma_8^2, \quad (31)$$

$$\mathcal{W} = 2 \ln \left( \frac{g\sqrt{\frac{4}{3}\sigma_0^2 + \frac{2\sqrt{2}}{3}\sigma_0\sigma_8 + \frac{5}{3}\sigma_8^2}}{\Lambda} \right) + \frac{1}{2}, \quad (32)$$

$$\mathcal{X} = 32\sigma_0^3 - 10\sqrt{2}\sigma_8^3 - 24\sqrt{2}\sigma_0^2\sigma_8 + 48\sigma_8^2\sigma_0, \quad (33)$$

$$\mathcal{Y} = 50\sigma_8^3 - 8\sqrt{2}\sigma_0^3 + 48\sigma_0^2\sigma_8 - 30\sqrt{2}\sigma_0\sigma_8^2, \quad (34)$$

$$\mathcal{Z} = \frac{4}{3}\sigma_0^2 - \frac{2\sqrt{2}}{3}\sigma_0\sigma_8 + \frac{5}{3}\sigma_8^2. \quad (35)$$

Rewriting everything according to Eq. (19) in terms of the physical fields, these mass corrections enter in the numerical routine to search for the vacuum parameters  $\lambda_1$  and  $m_0^2$ . These two parameters alone compensate for the vacuum contribution in the two condensate equations  $h_n$  and  $h_s$  in Eqs. (17).

It is interesting to note that the grand canonical potential remains unaffected by the choice of the renormalization scale parameter  $\Lambda_r$ . This is easily seen in the SU(2) case [39] and has also been shown for the SU(3) case for  $m_\sigma = 400$  MeV [28,42]. To compare our results with [42], the renormalization scale parameter is set to  $\Lambda_r = 200$  MeV.

## B. Charge neutrality and the gap equations

Since the lepton contribution decouples from the quark grand canonical potential, it can be treated separately. The electron contribution reads

$$\Omega_e = -\frac{2}{\beta} \int \frac{d^3k}{(2\pi)^3} \ln \left( 1 + e^{-\frac{E_{k,e} \pm \mu_e}{T}} \right) \quad (36)$$

with  $E_{k,e} = \sqrt{k^2 + m_e^2}$ , where  $m_e$  is the electron mass and  $\mu_e$  is the electron chemical potential.

A compact star is charge neutral, so that

$$\sum_{f=u,d,s,e} Q_f n_f = \frac{2}{3}n_u - \frac{1}{3}n_d - \frac{1}{3}n_s - n_e = 0 \quad (37)$$

with  $n_f$  as the particle density of each species  $f$ .

The total grand canonical potential is

$$\begin{aligned} \Omega^{\text{tot}} &= V - \frac{N_c N_f}{8\pi^2} \tilde{m}_f^4 \ln \left( \frac{\tilde{m}_f}{\Lambda_r} \right) - \frac{3}{\pi^2 \beta} \int_0^\infty k^2 dk \cdot \mathcal{N} \\ &\quad - \frac{2}{\beta} \int \frac{d^3k}{(2\pi)^3} \ln(1 + e^{-\frac{E_{k,e} \pm \mu_e}{T}}), \end{aligned} \quad (38)$$

and the vacuum parameter sets for different sigma meson mass  $m_\sigma$  are listed in Table I. As already mentioned, the potential is scale independent. The dependence cancels neatly, which is straightforward but tedious to check [28,39,42,43]. The independence of Eq. (38) on  $\Lambda_r$  in our work is checked numerically. The equations of motion

TABLE I. The vacuum parameters  $\lambda_1$ ,  $\lambda_2$ ,  $c$ ,  $m^2$ ,  $h_n$ , and  $h_s$  for different values of the sigma meson mass  $m_\sigma^{\text{vac}}$  in mean field approximation (MFA: upper table) and with the inclusion of the fermion vacuum term for the renormalization scale parameter  $\Lambda = 200$  MeV (eMFA: lower table).

$m_\sigma^{\text{vac}}$	$\Lambda$	$\lambda_1$	$\lambda_2$	$c$ [MeV]	$m^2$ [MeV <sup>2</sup> ]	$h_n$ [MeV <sup>3</sup> ]	$h_s$ [MeV <sup>3</sup> ]
400	...	-5.901	46.488	4807.245	(494.272) <sup>2</sup>	(120.73) <sup>3</sup>	(336.41) <sup>3</sup>
500	...	-2.698	46.488	4807.245	(434.541) <sup>2</sup>	(120.73) <sup>3</sup>	(336.41) <sup>3</sup>
600	...	1.398	46.488	4807.245	(342.496) <sup>2</sup>	(120.73) <sup>3</sup>	(336.41) <sup>3</sup>
700	...	6.615	46.488	4807.245	(161.918) <sup>2</sup>	(120.73) <sup>3</sup>	(336.41) <sup>3</sup>
800	...	13.488	46.488	4807.245	-(306.289) <sup>2</sup>	(120.73) <sup>3</sup>	(336.41) <sup>3</sup>
900	...	23.649	46.488	4807.245	-(520.82) <sup>2</sup>	(120.73) <sup>3</sup>	(336.41) <sup>3</sup>
$m_\sigma^{\text{vac}}$	$\Lambda$	$\lambda_1$	$\lambda_2$	$c$ [MeV]	$m^2$ [MeV <sup>2</sup> ]	$h_n$ [MeV <sup>3</sup> ]	$h_s$ [MeV <sup>3</sup> ]
400	200	-8.173	138.516	4807.245	(283.901) <sup>2</sup>	(120.73) <sup>3</sup>	(336.41) <sup>3</sup>
500	200	-5.285	138.516	4807.245	(173.694) <sup>2</sup>	(120.73) <sup>3</sup>	(336.41) <sup>3</sup>
600	200	-1.661	138.516	4807.245	-(181.951) <sup>2</sup>	(120.73) <sup>3</sup>	(336.41) <sup>3</sup>
700	200	2.819	138.516	4807.245	-(333.675) <sup>2</sup>	(120.73) <sup>3</sup>	(336.41) <sup>3</sup>
800	200	8.450	138.516	4807.245	-(457.902) <sup>2</sup>	(120.73) <sup>3</sup>	(336.41) <sup>3</sup>
900	200	16.179	138.516	4807.245	-(587.056) <sup>2</sup>	(120.73) <sup>3</sup>	(336.41) <sup>3</sup>

$$\frac{\partial \Omega^{\text{tot}}}{\partial \sigma_n} = \frac{\partial \Omega^{\text{tot}}}{\partial \sigma_s} = \frac{\partial \Omega^{\text{tot}}}{\partial \omega} = \frac{\partial \Omega^{\text{tot}}}{\partial \rho} = \frac{\partial \Omega^{\text{tot}}}{\partial \phi} \stackrel{!}{=} 0, \quad (39)$$

also known as the gap equations, finally determine the EoS,  $p(\epsilon)$ , with the pressure  $p$  and the energy density  $\epsilon$ .

### III. COMPACT STARS

The formalism discussed in the previous section can be used to obtain EoSs,  $p(\epsilon)$ , applicable for the calculation of compact stars. The resulting mass radius relations have to respect certain constraints to be physically reasonable. The most important constraints are the  $2 M_\odot$  limit [45–48] and the tidal deformability measurement by the LIGO/Virgo Collaboration [49,50].

#### A. Tidal deformability

The observation of the binary neutron star merger event GW170817 [49] is used to constrain the EoSs of compact stars [54–60,70–72]. During the inspiral phase, one star quadrupole deformation  $Q_{ij}$  in response to the companions perturbing tidal field  $\mathcal{E}_{ij}$  is measured by the tidal polarizability  $\lambda$ ,

$$Q_{ij} = -\lambda \mathcal{E}_{ij}. \quad (40)$$

$\lambda$  depends on the EoS [52,53,73] and is related to the stars quadrupolar tidal Love number [51]  $k_2$  via

$$k_2 = \frac{3}{2} \lambda R^{-5}, \quad (41)$$

where  $R$  is the radius of the star.

The Love number  $k_2$  is calculated as follows:

$$\begin{aligned} k_2 = & \frac{8C^5}{5} (1-2C)^2 [2 + 2C(y_R - 1) - y_R] \\ & \times \{2C[6 - 3y_R + 3C(5y_R - 8)] \\ & + 4C^3[13 - 11y_R + C(3y_R - 2) + 2C^2(1 + y_R)] \\ & + 3(1 - 2C)^2 [2 - y_R + 2C(y_R - 1)] \ln(1 - 2C)\}^{-1}, \end{aligned} \quad (42)$$

with the compactness  $C = M/R$ . The quantity  $y_R \equiv y(R)$  on the other hand is obtained by solving the differential equation for  $y(r)$  coming from the line element of the linearized metric, described in greater detail in [52,74,75]

$$\begin{aligned} & ry'(r) + y(r)^2 + r^2 Q(r) \\ & + y(r)e^{\lambda(r)} [1 + 4\pi r^2 (p(r) - \epsilon(r))] = 0, \end{aligned} \quad (43)$$

with

$$\begin{aligned} Q(r) = & 4\pi e^{\lambda(r)} \left( 5\epsilon(r) + 9p(r) + \frac{\epsilon(r) + p(r)}{c_s^2(r)} \right) \\ & - 6 \frac{e^{\lambda(r)}}{r^2} - (\nu'(r))^2, \end{aligned} \quad (44)$$

the metric functions from general relativity

$$e^{\lambda(r)} = \left( 1 - \frac{2m(r)}{r} \right)^{-1}, \quad (45)$$

$$\nu'(r) = 2e^{\lambda(r)} \frac{m(r) + 4\pi r^3 p(r)}{r^2}, \quad (46)$$

and  $c_s(r)^2 = dp/d\epsilon$  as the speed of sound squared [52,53,73]. The boundary condition of Eq. (43) is

$y(0) = 2$ , which implies no deformation at all in the center of the star. At the surface of a self-bound star  $c_s^2 \rightarrow 0$  and the denominator in Eq. (44) blows up. The density discontinuity leads to an extra expression just below the surface of the star [53,73,75]. One has to subtract

$$y_s = \frac{4\pi r^3 \epsilon_s(r)}{m(r)} \quad (47)$$

from Eq. (43) with  $\epsilon_s(r)$  being the value of the energy density just below the surface. The dimensionless tidal deformability  $\Lambda$  is

$$\Lambda = \frac{2k_2}{3C^5}, \quad (48)$$

usually solved simultaneously with the TOV equations [52,53,73]. The actual value of a  $1.4 M_\odot$  star has to be in a range  $\Lambda = 300_{-230}^{+420}$  [49,54].

#### IV. RESULTS

In this section we present our results for varying sigma meson mass  $m_\sigma$ , repulsive vector coupling  $g_\omega$ , and different values of the bag constant  $B^{1/4}$ . At the end of this section we compare the results from the eMFA with the MFA. The constituent quark mass is held fixed at  $m_q = 300$  MeV, which is roughly one-third of the nucleon mass. The standard parameter set is  $m_q = 300$  MeV,  $m_\sigma = 600$  MeV,  $g_\omega = 3.5$ , and  $B^{1/4} = 80$  MeV, in the following denoted as a reference set.

##### A. Variation of the sigma meson mass

Figure 1 shows the solutions of the scalar condensate equations, Eqs. (39), as a function of quark chemical

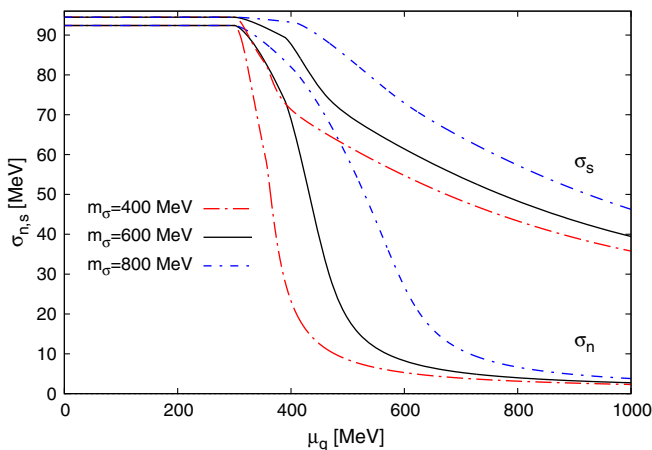


FIG. 1. The solutions of the condensate equations  $\sigma_n$  and  $\sigma_s$  in the extended mean field approximation as a function of the quark chemical potential  $\mu_q$  for different values of  $m_\sigma$ . The other parameters are  $m_q = 300$  MeV,  $g_\omega = 3.5$ , and  $B^{1/4} = 80$  MeV.

potential  $\mu_q$  for the scalar fields  $\sigma_n$  and  $\sigma_s$ . For all our choices of  $m_\sigma$  a crossover transition is found. For larger values of  $m_\sigma$  the restoration of chiral symmetry happens at larger quark chemical potential  $\mu_q$  than for a lower mass of the sigma meson. A first order phase transition in the eMFA within this parameter choice is not found. Chiral symmetry is not entirely restored, because of the explicit breaking of chiral symmetry [16,32].

Figure 2 shows the EoSs for three different values of the sigma meson mass, 400 MeV, 600 MeV, and 800 MeV. The symbol on a particular EoS denotes the corresponding location of the maximum mass star on the EoS. The red circle marks the maximum mass star on the EoS for  $m_\sigma = 400$  MeV. The black triangle is the maximum mass star on the reference set, and the blue square is the representative maximum mass star for  $m_\sigma = 800$  MeV. The corresponding vacuum parameters are listed in Table I. Due to the implementation of the fermion vacuum term the behavior of the grand potential, Eq. (5), i.e., the resulting EoS, is highly nonlinear. The appropriate EoSs stiffen with increasing sigma meson mass  $m_\sigma$  for  $p \leq 100$  MeV/fm<sup>3</sup>, which is in contrast to the MFA case [16]. For  $p \geq 100$  MeV/fm<sup>3</sup> the EoSs stiffen with decreasing sigma meson mass  $m_\sigma$  as in the MFA. The inset of Fig. 2 shows the crossing of the EoSs where the EoS for  $m_\sigma = 400$  MeV crosses the  $m_\sigma = 600$  MeV EoS at  $p = 20$  MeV/fm<sup>3</sup> and then the  $m_\sigma = 800$  MeV EoS at  $p = 35$  MeV/fm<sup>3</sup>.

The corresponding speed of sound  $c_s^2$  for the different choices of  $m_\sigma$  can be seen in Fig. 3. The inset displays that the speed of sound approaches  $c_s^2 = 0.5$  at large energy densities. The EoS for  $m_\sigma = 400$  MeV generates the highest values of the speed of sound  $c_s^2$  at a given energy density for values of the energy density  $\epsilon \geq 220$  MeV/fm<sup>3</sup>.

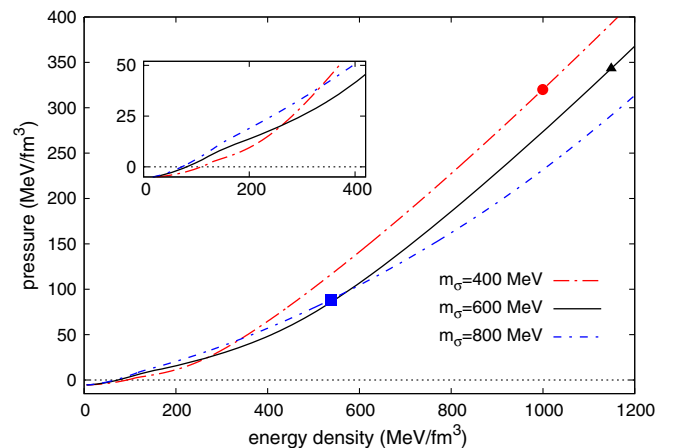


FIG. 2. The EoSs for different values of the sigma meson mass  $m_\sigma$ . The inlaid figure accentuates the behavior at rather low energies, resulting in nontrivial mass-radius sequences. The symbols indicate where the maximum mass star is located on the respective EoS. The other parameters are  $m_q = 300$  MeV,  $g_\omega = 3.5$ , and  $B^{1/4} = 80$  MeV.

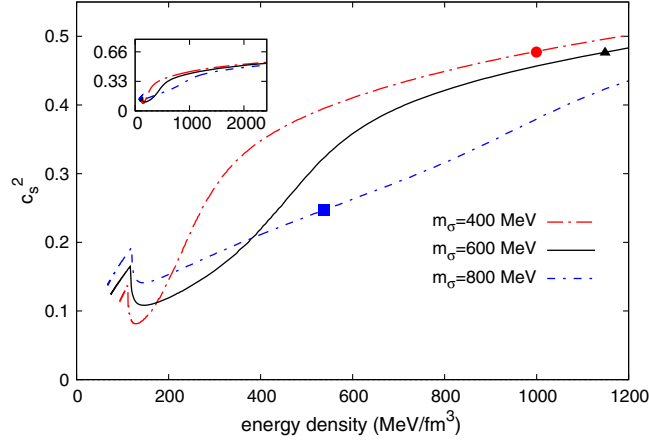


FIG. 3. The speed of sound for different values of the sigma meson mass  $m_\sigma$ . The symbols indicate the maximum mass star. The inset shows that the speed of sound approaches  $c_s^2 = 0.5$  for large energy densities. The other parameters are  $m_q = 300$  MeV,  $g_\omega = 3.5$ , and  $B^{1/4} = 80$  MeV.

This feature results from the stiffness of the EoS; see also Fig. 2.  $c_s^2$  influences the solution of the differential equation, Eq. (43), via the quantity  $Q(r)$ , Eq. (44). Thereby  $k_2$  and eventually the tidal deformability  $\Lambda$ , Eq. (48), are influenced by the EoS.

The mass radius relations can be seen in Fig. 4, where for our parameter choices  $2 M_\odot$  are possible [45–48], indicated by the upper horizontal line. The lower horizontal line indicates  $1.4 M_\odot$ . For the lowest value of  $m_\sigma = 400$  MeV chosen in this article, the mass radius relation is more compact than for the other choices of  $m_\sigma$ . This feature is different in the MFA [16] and results from the

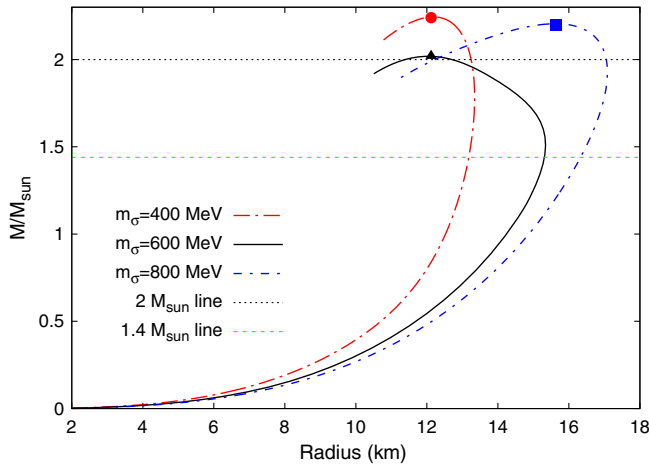


FIG. 4. The mass radius relation for different values of the sigma meson mass  $m_\sigma$ . For  $m_\sigma = 400$  MeV the maximum mass is  $2.24 M_\odot$  at  $12.12$  km, for  $m_\sigma = 600$  MeV  $2 M_\odot$  are reached at the same radius, whereas for  $m_\sigma = 800$  MeV the maximum mass is  $2.2 M_\odot$  at  $15.65$  km radius. These values are also listed in Table II. The other parameters are  $m_q = 300$  MeV,  $g_\omega = 3.5$ , and  $B^{1/4} = 80$  MeV.

nontrivial behavior of the EoSs discussed for Fig. 2. At  $m_\sigma = 400$  MeV the radius of a  $1.4 M_\odot$  star is  $R_{1.4 M_\odot} = 13.14$  km, whereas for  $m_\sigma = 600$  MeV  $R_{1.4 M_\odot} = 15.27$  km and for  $m_\sigma = 800$  MeV  $R_{1.4 M_\odot} = 16.22$  km (see also Table II). With increasing  $m_\sigma$  the configurations become less compact, but nonetheless has the mass radius relation for  $m_\sigma = 600$  MeV, the smallest maximum mass of  $2.02 M_\odot$ . This value is at roughly the same radius  $R = 12.12$  km as the mass radius relation for  $m_\sigma = 400$  MeV with a maximum value of  $2.24 M_\odot$ . The maximum mass for  $m_\sigma = 800$  MeV is  $2.2 M_\odot$  at a radius  $R = 15.65$  km. It is, however, not seen in the MFA that the maximum masses for two different values of  $m_\sigma = 400$  MeV and  $m_\sigma = 800$  MeV are nearly equal at different radii. This peculiarity can be explained with the nontrivial behavior of the EoSs for  $p \leq 100$  MeV/fm<sup>3</sup>; see inset of Fig. 2.

Figure 5 shows the radial profile of the maximum mass star with  $M = 2.02 M_\odot$  at  $R = 12.12$  km from the standard parameter set, i.e., the black triangles in Figs. 2, 3, and 4. The left figure displays the nonstrange  $\sigma_n$  and the strange  $\sigma_s$  condensate as a function of the stars' radius  $R$ . The right figure shows the pressure  $p$  and the energy density  $\epsilon$  as a function of the stars' radius  $R$ . The curves are rather smooth because the phase transition is a crossover. The nonstrange  $\sigma_n$  condensate has a value below  $10$  MeV/fm<sup>3</sup> in the center of the star at  $R = 0$ , which is a magnitude smaller than the value of the chirally broken phase  $f_\pi = 92.4$  MeV. However, chiral symmetry is not fully restored in the center of the  $2.02 M_\odot$  star as the strange  $\sigma_s$  condensate at  $R = 0$  is only slightly below  $60$  MeV for a vacuum expectation value of  $94.47$  MeV.

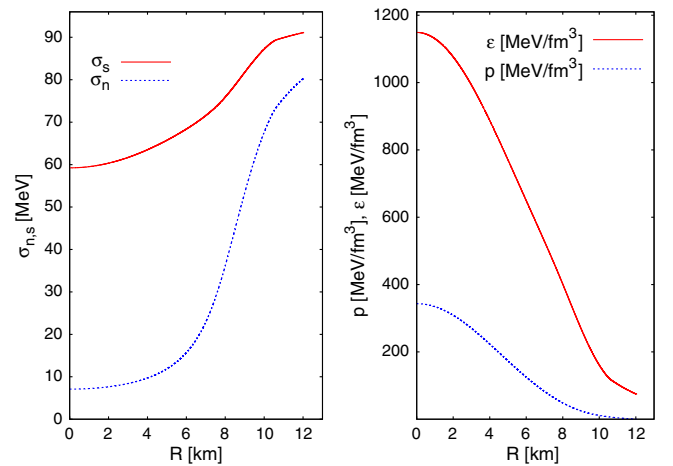


FIG. 5. The radial profile of the maximum mass star with  $M = 2.02 M_\odot$  at  $R = 12.12$  km (the black triangle) from the standard parameter set  $m_q = 300$  MeV,  $m_\sigma = 600$  MeV,  $g_\omega = 3.5$ , and  $B^{1/4} = 80$  MeV. The left figure displays the nonstrange and the strange  $\sigma$  condensate as a function of the stars' radius  $R$ . The right figure shows the pressure  $p$  and energy density  $\epsilon$  as a function of the stars' radius  $R$ .

TABLE II. eMFA: The values of the radius at  $1.4 M_{\odot}$ , the tidal deformability parameter  $\Lambda_{1.4 M_{\odot}}$ , the maximum radius, the maximum mass, and the central pressure and central energy density for the maximum mass stars for the parameters  $m_{\sigma}$ ,  $g_{\omega}$ , and  $B^{1/4}$ .

$m_{\sigma}$ [MeV]	$g_{\omega}$	$B^{1/4}$ [MeV]	$R_{1.4 M_{\odot}}$ [km]	$\Lambda_{1.4 M_{\odot}}$	$R_{\max}$ [km]	$M_{\max}$ [ $M_{\odot}$ ]	$p_{\max}$ [MeV/fm <sup>3</sup> ]	$\epsilon_{\max}$ [MeV/fm <sup>3</sup> ]
400	3.5	80	13.14	1107	12.12	2.24	320.02	999.55
600	3.5	80	15.27	3253	12.12	2.02	343.21	1148.82
800	3.5	80	16.22	5184	15.65	2.20	88.62	537.67
600	1	80	9.32	47	8.87	1.44	409.65	1829.86
600	6	80	18.06	1079	17.15	2.82	128.35	509.77
600	3.5	50	22.57	5250	22.80	2.61	23.35	221.13
600	3.5	110	10.10	66	9.36	1.79	578.83	1658.17

TABLE III. MFA: The values of the radius at  $1.4 M_{\odot}$ , the tidal deformability parameter  $\Lambda_{1.4 M_{\odot}}$ , the maximum radius, the maximum mass, and the central pressure and central energy density for the maximum mass stars for the parameters  $m_{\sigma}$ ,  $g_{\omega}$ , and  $B^{1/4}$ .

$m_{\sigma}$ [MeV]	$g_{\omega}$	$B^{1/4}$ [MeV]	$R_{1.4 M_{\odot}}$ [km]	$\Lambda_{1.4 M_{\odot}}$	$R_{\max}$ [km]	$M_{\max}$ [ $M_{\odot}$ ]	$p_{\max}$ [MeV/fm <sup>3</sup> ]	$\epsilon_{\max}$ [MeV/fm <sup>3</sup> ]
400	3.5	80	14.38	2275	15.28	2.70	142.70	568.15
600	3.5	80	12.51	680	11.47	2.03	330.56	1143.22
800	3.5	80	16.10	4858	15.88	2.09	64.78	480.79
600	1	80	10.74	389	10.45	1.71	206.77	1091.38
600	6	80	18.00	9815	14.86	2.58	251.90	761.90
600	3.5	50	21.92	25300	14.5	2.19	228.14	878.17
600	3.5	110	10.08	243	9.61	1.82	467.07	1493.87

## B. Comparison with the mean field approximation

The stars on the mass radius relation for a larger value of the repulsive coupling parameter  $g_{\omega}$  have larger maximum masses and also larger radii, which is qualitatively known from the MFA case [14,16]; see also the corresponding values in Table II for the eMFA and Table III for the MFA.

The vacuum pressure constant  $B^{1/4}$  drops out in the equations of motion, Eqs. (39) and (6), respectively. Smaller values of  $B^{1/4}$  have essentially the same effect on the mass radius relation as a larger repulsive coupling  $g_{\omega}$ : Maximum masses and radii become larger.

Figure 6 shows contour lines of  $2 M_{\odot}$  maximum mass for the MFA and the eMFA cases at fixed  $g_{\omega} = 2.5, 3,$  and  $3.5$  in the  $m_{\sigma}$  vs  $B^{1/4}$  plane. For a parameter choice on the right-hand side of a particular contour line, the maximum mass of the corresponding mass radius relation is smaller than  $2 M_{\odot}$ , and on the left-hand side consequently larger than  $2 M_{\odot}$ . Furthermore, smaller values of the repulsive coupling  $g_{\omega}$  together with a relatively small value of the vacuum pressure constant  $B^{1/4}$  yield maximum masses of  $\geq 2 M_{\odot}$  in the mass radius relation [16,18]. This statement holds for the MFA and for the eMFA cases.

The contour lines of the MFA and the eMFA seem somehow to be shifted vertically with a difference of  $m_{\sigma} \simeq 150$  MeV for  $g_{\omega} = 2.5$ ,  $m_{\sigma} \simeq 100$  MeV for  $g_{\omega} = 3.0$ , and  $m_{\sigma} \simeq 50$  MeV for  $g_{\omega} = 3.5$ . The difference in the shift in  $m_{\sigma}$  becomes smaller for larger values of  $g_{\omega}$ . For a certain  $m_{\sigma} \leq 620$  MeV, larger values of  $B^{1/4}$  are allowed for  $2 M_{\odot}$  in the MFA compared to the eMFA, resulting in more

compact mass radius relations in the MFA. Recall that smaller values of  $B^{1/4}$  generate rather larger radii, so that denser stars yield smaller values of the tidal deformability parameter  $\Lambda \propto C^{-5}$  [see Eq. (48)]. For at least  $2 M_{\odot}$  in the eMFA with values  $m_{\sigma} \geq 620$  MeV a rather large value of  $B^{1/4}$  is necessary. The mass radius configurations, however, turn out to already have a too large radius for a small tidal

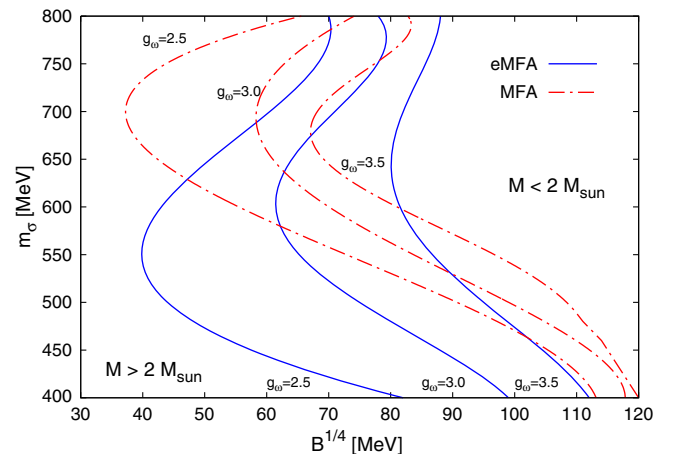


FIG. 6. Contour lines of maximum masses of  $2 M_{\odot}$  in the  $m_{\sigma}$  vs  $B^{1/4}$  plane for fixed  $2.5 \leq g_{\omega} \leq 3.5$ . Smaller values of the repulsive coupling  $g_{\omega}$  accompanied with a relatively small value of the vacuum pressure  $B^{1/4}$  yields a maximum mass of  $2 M_{\odot}$  in the mass radius relation. This holds for the MFA (dashed lines) and for the eMFA (continuous lines).

deformability parameter  $\Lambda \leq 720$ ; see also Table II for the eMFA and Table III for the MFA.

Figure 7 shows contour lines of maximum masses of  $2 M_\odot$  for the MFA and the eMFA cases at fixed  $B^{1/4}$  in the  $m_\sigma$  vs  $g_\omega$  plane. For a particular parameter choice the maximum mass is larger than  $2 M_\odot$  on the right-hand side of a particular contour line and on the left-hand side consequently smaller. Recall that a larger value of the repulsive coupling is needed for  $2 M_\odot$  at fixed vacuum pressure constant  $B^{1/4}$ .

It is interesting to note that in the MFA case no repulsive coupling is necessary to generate two solar masses for rather small  $m_\sigma$ , making the configurations more compact compared to the eMFA case. As already mentioned, more compact configurations are in favor of a low value of the tidal deformability parameter  $\Lambda$ .

Figure 8 shows the value of the tidal deformability parameter  $\Lambda$  according to Eq. (48) on a logarithmic scale for a  $1.4 M_\odot$  star as a function of the radius of a  $1.4 M_\odot$  star. The shaded area fulfills both constraints on either  $R \leq 13.5$  km [54–61] or  $\Lambda \leq 720$  [50]. The  $c_s^2$  curve corresponds to the MIT bag model EoS  $p = c_s^2 \epsilon - 4B$  and is obtained for different values of the vacuum pressure constant  $B$ . It is interesting to note that the curves for the MIT bag model for  $c_s^2 = 1$  and  $c_s^2 = 1/3$  are relatively close together. This feature indicates that a particular function  $\Lambda_{1.4 M_\odot}(R_{1.4 M_\odot})$  is rather independent of the speed of sound  $c_s^2$ , so that  $c_s^2$  in Eq. (44) plays a subdominant part. The curve for  $c_s^2 = 1$  can also be seen as an upper limit due to causality.

The MFA and the eMFA cases are obtained by varying  $m_\sigma$  in the standard parameter set. In the eMFA case the  $\Lambda_{1.4 M_\odot}$  values and the radii decrease linearly on the

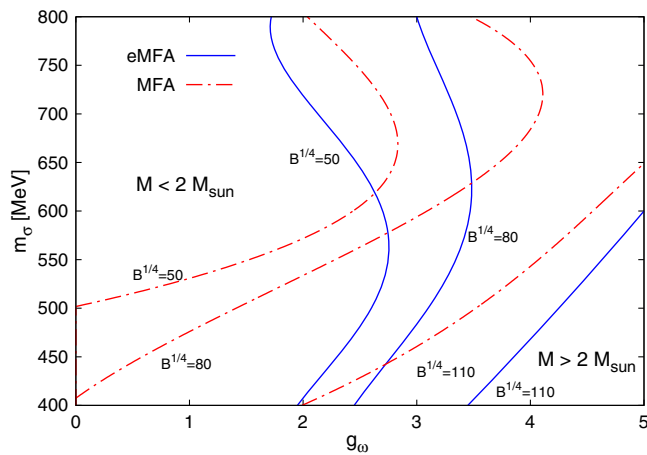


FIG. 7. Contour lines of maximum masses of  $2 M_\odot$  in the  $m_\sigma$  vs  $g_\omega$  plane at fixed  $50 \text{ MeV} \leq B^{1/4} \leq 110 \text{ MeV}$ . In the MFA case (dotted lines) no repulsive coupling is necessary to generate two solar masses for low  $m_\sigma$ . The configurations in MFA are more compact compared to the eMFA case (continuous lines).

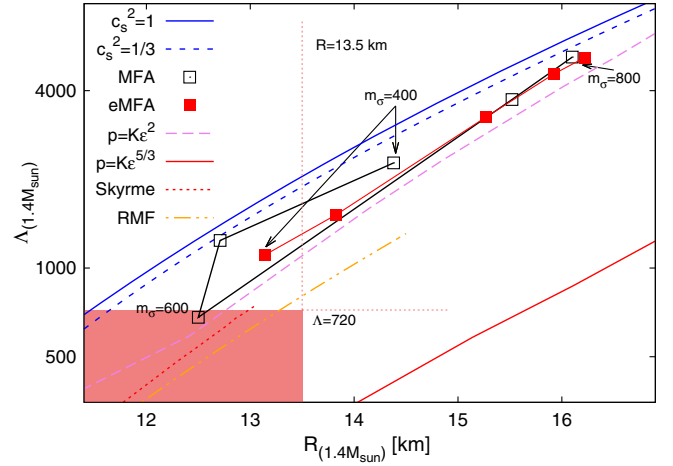


FIG. 8. The values of the tidal deformability parameter  $\Lambda$  on a logarithmic scale for a  $1.4 M_\odot$  star as a function of the radius for a  $1.4 M_\odot$  star for various EoSs. The shaded area fulfills both constraints on either  $R \leq 13.5$  km or  $\Lambda \leq 720$ .

logarithmic scale with decreasing  $m_\sigma$  (see also Table II). In the MFA case a minimum value  $\Lambda = 680$  at  $12.51$  km radius for  $m_\sigma = 600$  MeV is found (see also Table III). Smaller and larger values of  $m_\sigma = 600$  MeV lead to larger values of either  $\Lambda_{1.4 M_\odot}$  or the corresponding radius. This feature may be explained due to a shift in the dominance of attractive and repulsive field contributions to the stiffness of the EoS, and has already been suspected and discussed in [16]. The only parameter set which respects the  $2 M_\odot$  limit, the  $R_{1.4 M_\odot} \leq 13.5$  km bound, and the  $\Lambda_{1.4 M_\odot} \leq 720$  constraint is the reference set in the MFA and is hence located within the shaded area in Fig. 8.

The inclusion of the fermion vacuum term in the SU(3) chiral quark meson model seems not to be compatible with astrophysical measurements and constraints.

To sort our results for the SU(3) quark meson model within other approaches, a Skyrme parameter approach taken from Zhou *et al.* [76] and an relativistic mean field (RMF) model studied by Nandi *et al.* [77] are included in Fig. 8. The RMF values correspond to the fit function  $\Lambda_{1.4 M_\odot} = 1.53 \times 10^{-5} (R_{1.4 M_\odot}/\text{km})^{6.83}$  [77]. The values of these two approaches are located at smaller  $\Lambda_{1.4 M_\odot}$  at a given radius and lie well within the shaded area. Furthermore, the results for free Fermi gas EoSs  $p = K \epsilon^{1+1/n}$  for various constants  $K$ , with  $n = 1$  and  $n = 3/2$  are also shown. The values of  $\Lambda_{1.4 M_\odot}(R_{1.4 M_\odot})$  for the interaction dominated EoS with  $n = 1$  lie in between the results of the quark matter EoSs and the Skyrme and RMF approach. The results of the nonrelativistic EoS for  $n = 3/2$  may be seen as a lower limit for the function  $\Lambda_{1.4 M_\odot}(R_{1.4 M_\odot})$  in Fig. 8. The values for  $\Lambda_{1.4 M_\odot}$  at a given radius of the hadronic EoSs are located above the values of the nonrelativistic EoS.

In general it seems that stars composed of quark matter have larger values of the tidal deformability parameter  $\Lambda$

for a  $1.4 M_{\odot}$  star at a given radius than stars generated by hadronic EoSs.

## V. CONCLUSIONS

We have studied the SU(3) quark meson model including the fermion vacuum term and have determined the vacuum parameters for different values of the sigma meson mass  $m_{\sigma}$ . The whole potential is independent of any renormalization scale [28,31,42,43].

For all scalar meson masses in the eMFA a crossover transition in the condensates is found. In general it seems that in the MFA a first order phase transition is possible in a larger parameter space. For larger values of  $m_{\sigma}$  the restoration of chiral symmetry happens at the larger quark chemical potential  $\mu_q$  [78], which is also observed for larger values of  $g_{\omega}$ . The bag constant  $B^{1/4}$  on the other hand does not affect the condensates at all, since it drops out in the equations of motion.

The resulting EoSs have been used to calculate mass radius relations of compact stars. These mass radius relations have to respect the  $2 M_{\odot}$  limit [45–48] and the constraints coming from the analysis of the tidal deformabilities of the GW170817 neutron star merger event [50,54–60]. We compare our results from the eMFA with the MFA. Our finding is that the  $2 M_{\odot}$  constraint can be fulfilled in both approaches in a rather wide parameter space (see, e.g., [16]), and that in the eMFA the mass radius relations are generally less compact resulting in larger values of the tidal deformability parameter  $\Lambda$ . This feature, however, implies that in the eMFA the constraints from GW170817 are not fulfilled, i.e.,  $\Lambda_{1.4 M_{\odot}} \geq 720$ . In the MFA a small parameter space is found where all considered restrictions are satisfied.

Within our parameter choice in the eMFA a smaller value of the sigma meson mass  $m_{\sigma}$  is favored for a rather compact mass radius relation. This is in contrast to the MFA (see, e.g., [16]), and may be explained via the additional term in the potential resulting from the fermion vacuum contribution.

A large repulsive coupling constant  $g_{\omega}$  stiffens the EoS and hence enables the star to generate more pressure against gravity. The maximum mass and also the radius become consequently larger. These features may then result in larger values for the tidal deformability parameter  $\Lambda \propto C^{-5}$ ,  $C$  being the compactness. Incidentally, this holds vice versa; i.e., small repulsive couplings  $g_{\omega}$  imply rather small tidal deformabilities, but the  $2 M_{\odot}$  constraint may not be fulfilled.

The EoSs substantially soften when increasing the vacuum pressure constant  $B^{1/4}$  so that for values  $B^{1/4} \geq 110$  MeV maximum masses of  $2 M_{\odot}$  are difficult to obtain. Smaller values of  $B^{1/4}$ , on the other hand, have essentially

the same effect on the mass radius relation as a larger repulsive coupling  $g_{\omega}$ ; i.e., maximum masses and radii become larger and consequently so does the tidal deformability parameter  $\Lambda$ .

To sort our results we compare our findings for the tidal deformability parameter at  $1.4 M_{\odot}$ ,  $\Lambda_{1.4 M_{\odot}}(R_{1.4 M_{\odot}})$ , with the results for a constant speed of sound (linear) EoS with  $c_s^2 = 1$ , where  $M \propto R^3$  and which can be seen as an upper limit due to causality. As a lower limit we introduce a nonrelativistic polytropic EoS with the polytropic index  $\Gamma = 5/3$  where  $M \propto R^{-3}$ . The case  $\Gamma = 2$  corresponds to an interaction dominated EoS where  $R \simeq \text{const}$ , independent of the mass of the stars on the mass radius relation. In between these results we find the results of the MFA and eMFA cases relatively close to the constant speed of sound EoSs and the polytrope  $n = 2$ . For further comparison we also took a Skyrme parameter approach taken from Zhou *et al.* [76] and an RMF model studied by Nandi *et al.* [77]. Their results are located slightly below the values of the polytropic  $\Gamma = 2$  case and centrally in between the results from the constant speed of sound and the nonrelativistic polytropic EoS.

In general it seems that quark matter stars have larger values of the tidal deformability parameter  $\Lambda$  at  $1.4 M_{\odot}$  than hadronic stars. Taking into account more interactions among quarks could lower the value of the tidal deformability parameter  $\Lambda_{1.4 M_{\odot}}(R_{1.4 M_{\odot}})$ , because interactions among quarks may decrease the value of  $\Lambda_{1.4 M_{\odot}}$  at a given radius; see Fig. 8.

A first order chiral phase transition yielding twin stars as in the MFA (see, e.g., [18]) was not found in the eMFA. Compared to the mean field case, the EoSs show a smooth behavior due to the additional term in the potential coming from the fermion vacuum term. The MFA and the eMFA, however, yield stars with  $\geq 2 M_{\odot}$  and radii  $\leq 13.5$  km at  $1.4 M_{\odot}$ , but only in the MFA was the additional  $\Lambda \leq 720$  limit fulfilled for one set of parameters, i.e., for  $m_{\sigma} = 600$  MeV. This is due to the fact that the MFA approach yields more compact mass radius relations than the eMFA case. In the eMFA the  $2 M_{\odot}$  limit is fulfilled for the most compact mass radius configuration at  $m_{\sigma} = 400$  MeV with a radius of 13.14 km, but the value of  $\Lambda_{1.4 M_{\odot}}(R_{1.4 M_{\odot}}) = 1107$  is not compatible with GW170817.

## ACKNOWLEDGMENTS

The authors thank Jan-Erik Christian for fruitful discussions on the tidal deformability. J.S. and A.Z. acknowledge support from the Hessian LOEWE initiative through the Helmholtz International Center for FAIR (HIC for FAIR).

- [1] S. Gasiorowicz and D. A. Geffen, *Rev. Mod. Phys.* **41**, 531 (1969).
- [2] V. Koch, *Int. J. Mod. Phys. E* **06**, 203 (1997).
- [3] F. Karsch, E. Laermann, and A. Peikert, *Nucl. Phys.* **B605**, 579 (2001).
- [4] D. Zschiesche, P. Papazoglou, S. Schramm, C. Beckmann, J. Schaffner-Bielich, H. Stöcker, and W. Greiner, *Springer Tracts Mod. Phys.* **163**, 129 (2000).
- [5] D. Parganlija, P. Kovacs, G. Wolf, F. Giacosa, and D. Rischke, *AIP Conf. Proc.* **1520**, 226 (2013).
- [6] D. Parganlija, P. Kovacs, G. Wolf, F. Giacosa, and D. H. Rischke, *Phys. Rev. D* **87**, 014011 (2013).
- [7] S. Gavin, A. Goksch, and R. D. Pisarski, *Phys. Rev. D* **49**, R3079 (1994).
- [8] S. Chandrasekharan, D. Chen, N. Christ, W. Lee, R. Mawhinney, and P. Vranas, *Phys. Rev. Lett.* **82**, 2463 (1999).
- [9] D. A. Kirzhnits and A. D. Linde, *Phys. Lett. B* **42**, 471 (1972).
- [10] R. D. Pisarski and F. Wilczek, *Phys. Rev. D* **29**, 338 (1984).
- [11] L. Zduunik, R. Schaeffer, and P. Haensel, *Astron. Astrophys. Rev.*, **126**, 121 (1983).
- [12] I. Sagert, G. Pagliara, M. Hempel, and J. Schaffner-Bielich, *J. Phys. G* **35**, 104079 (2008).
- [13] J. Schaffner-Bielich, *Nucl. Phys.* **A835**, 279 (2010).
- [14] S. Weissenborn, D. Chatterjee, and J. Schaffner-Bielich, *Phys. Rev. C* **85**, 065802 (2012).
- [15] D. Blaschke and D. E. Alvarez-Castillo, *AIP Conf. Proc.* **1701**, 020013 (2016).
- [16] A. Zacchi, R. Stiele, and J. Schaffner-Bielich, *Phys. Rev. D* **92**, 045022 (2015).
- [17] A. Zacchi, M. Hanauske, and J. Schaffner-Bielich, *Phys. Rev. D* **93**, 065011 (2016).
- [18] A. Zacchi, L. Tolos, and J. Schaffner-Bielich, *Phys. Rev. D* **95**, 103008 (2017).
- [19] T. Toimela, *Int. J. Theor. Phys.* **24**, 901 (1985).
- [20] A. Mocsy, I. N. Mishustin, and P. J. Ellis, *Phys. Rev. C* **70**, 015204 (2004).
- [21] E. Braaten and A. Nieto, *Phys. Rev. Lett.* **76**, 1417 (1996).
- [22] E. S. Fraga and P. Romatschke, *Phys. Rev. D* **71**, 105014 (2005).
- [23] D. Parganlija and F. Giacosa, *Eur. Phys. J. C* **77**, 450 (2017).
- [24] J. B. Kogut, M. Stone, H. W. Wyld, S. Shenker, J. Shigemitsu, and D. K. Sinclair, *Nucl. Phys.* **B225**, 326 (1983).
- [25] V. Koch, *Phys. Lett. B* **351**, 29 (1995).
- [26] B.-J. Schaefer and J. Wambach, *Nucl. Phys.* **A757**, 479 (2005).
- [27] D. Parganlija, F. Giacosa, and D. H. Rischke, *Phys. Rev. D* **82**, 054024 (2010).
- [28] U. S. Gupta and V. K. Tiwari, *Phys. Rev. D* **85**, 014010 (2012).
- [29] T. K. Herbst, M. Mitter, J. M. Pawłowski, B.-J. Schaefer, and R. Stiele, *Phys. Lett. B* **731**, 248 (2014).
- [30] R. Stiele, E. S. Fraga, and J. Schaffner-Bielich, *Phys. Lett. B* **729**, 72 (2014).
- [31] J. T. Lenaghan and D. H. Rischke, *J. Phys. G* **26**, 431 (2000).
- [32] J. T. Lenaghan, D. H. Rischke, and J. Schaffner-Bielich, *Phys. Rev. D* **62**, 085008 (2000).
- [33] M. Grahl, E. Seel, F. Giacosa, and D. H. Rischke, *Phys. Rev. D* **87**, 096014 (2013).
- [34] E. Seel, S. Struber, F. Giacosa, and D. H. Rischke, *Phys. Rev. D* **86**, 125010 (2012).
- [35] Y. Hara, Y. Nambu, and J. Schechter, *Phys. Rev. Lett.* **16**, 380 (1966).
- [36] V. Bernard, A. H. Blin, B. Hiller, Y. P. Ivanov, A. A. Osipov, and U.-G. Meißner, *Ann. Phys. (N.Y.)* **249**, 499 (1996).
- [37] K. Schertler, S. Leupold, and J. Schaffner-Bielich, *Phys. Rev. C* **60**, 025801 (1999).
- [38] M. Buballa, *Phys. Rep.* **407**, 205 (2005).
- [39] A. Zacchi and J. Schaffner-Bielich, *Phys. Rev. D* **97**, 074011 (2018).
- [40] E. S. Fraga, L. F. Palhares, and M. B. Pinto, *Phys. Rev. D* **79**, 065026 (2009).
- [41] V. Skokov, B. Friman, E. Nakano, K. Redlich, and B. J. Schaefer, *Phys. Rev. D* **82**, 034029 (2010).
- [42] S. Chatterjee and K. A. Mohan, *Phys. Rev. D* **85**, 074018 (2012).
- [43] V. K. Tiwari, *Phys. Rev. D* **88**, 074017 (2013).
- [44] R. C. Tolman, *Phys. Rev.* **55**, 364 (1939).
- [45] P. Demorest, T. Pennucci, S. Ransom, M. Roberts, and J. Hessels, *Nature (London)* **467**, 1081 (2010).
- [46] J. Antoniadis *et al.*, *Science* **340**, 1233232 (2013).
- [47] E. Fonseca *et al.*, *Astrophys. J.* **832**, 167 (2016).
- [48] H. T. Cromartie *et al.*, arXiv:1904.06759.
- [49] B. Abbott *et al.* (LIGO Scientific, Virgo Collaborations), *Phys. Rev. Lett.* **119**, 161101 (2017).
- [50] B. P. Abbott *et al.* (LIGO Scientific, Virgo Collaborations), *Phys. Rev. X* **9**, 011001 (2019).
- [51] A. E. H. Love, *Proc. R. Soc. A* **82**, 551 (1908).
- [52] T. Hinderer, *Astrophys. J.* **677**, 1216 (2008).
- [53] S. Postnikov, M. Prakash, and J. M. Lattimer, *Phys. Rev. D* **82**, 024016 (2010).
- [54] B. P. Abbott *et al.* (LIGO Scientific, Virgo Collaborations), *Phys. Rev. Lett.* **121**, 161101 (2018).
- [55] E. R. Most, L. R. Weih, L. Rezzolla, and J. Schaffner-Bielich, *Phys. Rev. Lett.* **120**, 261103 (2018).
- [56] E. Annala, T. Gorda, A. Kurkela, and A. Vuorinen, *Phys. Rev. Lett.* **120**, 172703 (2018).
- [57] S. De, D. Finstad, J. M. Lattimer, D. A. Brown, E. Berger, and C. M. Biwer, *Phys. Rev. Lett.* **121**, 091102 (2018).
- [58] B. Kumar, B. K. Agrawal, and S. K. Patra, *Phys. Rev. C* **97**, 045806 (2018).
- [59] F. J. Fattoyev, J. Piekarewicz, and C. J. Horowitz, *Phys. Rev. Lett.* **120**, 172702 (2018).
- [60] T. Malik, N. Alam, M. Fortin, C. Providencia, B. K. Agrawal, T. K. Jha, B. Kumar, and S. K. Patra, *Phys. Rev. C* **98**, 035804 (2018).
- [61] N. Hornick, L. Tolos, A. Zacchi, J.-E. Christian, and J. Schaffner-Bielich, *Phys. Rev. C* **98**, 065804 (2018).
- [62] B.-J. Schaefer and M. Wagner, *Phys. Rev. D* **79**, 014018 (2009).
- [63] T. Beisitzer, R. Stiele, and J. Schaffner-Bielich, *Phys. Rev. D* **90**, 085001 (2014).
- [64] A. R. Bodmer, *Phys. Rev. D* **4**, 1601 (1971).
- [65] A. Chodos, R. L. Jaffe, K. Johnson, C. B. Thorn, and V. F. Weisskopf, *Phys. Rev. D* **9**, 3471 (1974).
- [66] E. Farhi and R. L. Jaffe, *Phys. Rev. D* **30**, 2379 (1984).
- [67] E. Witten, *Phys. Rev. D* **30**, 272 (1984).

- [68] K. A. Olive *et al.* (Particle Data Group), *Chin. Phys. C* **38**, 090001 (2014).
- [69] M. Y. Ishida, *Nucl. Phys.* **A629**, 148c (1998).
- [70] D. Radice, A. Perego, F. Zappa, and S. Bernuzzi, *Astrophys. J.* **852**, L29 (2018).
- [71] B. Margalit and B. D. Metzger, *Astrophys. J.* **850**, L19 (2017).
- [72] L. Rezzolla, E. R. Most, and L. R. Weih, *Astrophys. J.* **852**, L25 (2018).
- [73] T. Hinderer, B. D. Lackey, R. N. Lang, and J. S. Read, *Phys. Rev. D* **81**, 123016 (2010).
- [74] K. S. Thorne and A. Campolattaro, *Astrophys. J.* **149**, 591 (1967).
- [75] T. Damour and A. Nagar, *Phys. Rev. D* **80**, 084035 (2009).
- [76] Y. Zhou, L.-W. Chen, and Z. Zhang, *Phys. Rev. D* **99**, 121301 (2019).
- [77] R. Nandi, P. Char, and S. Pal, *Phys. Rev. C* **99**, 052802 (2019).
- [78] S. Han and A. W. Steiner, *Phys. Rev. D* **99**, 083014 (2019).